Impact of urbanized atmosphere-land processing to the near-ground distribution of air pollution over Central Liaoning Urban Agglomeration

Wenxi Zhang [a], Zhenxin Liu [a,*], Xiaolan Li [a,b], Yuhao Mao [a], Yanjun Ma [b], Hong Liao [a]

[a] *Jiangsu Key Laboratory of Atmospheric Environment Monitoring and Pollution Control/Jiangsu Collaborative Innovation Center of Atmospheric Environment and Equipment Technology, School of Environmental Science and Engineering, Nanjing University of Information Science and Technology (NUIST), Nanjing, 210044, China*
[b] *Institute of Atmospheric Environment, China Meteorological Administration, Shenyang, Liaoning, 110166, China*

HIGHLIGHTS

- Urbanization has a significant influence on the spatial and temporal distribution of air pollutants.
- Numerical experiments proved the pollutant transport in urban areas affected by the land surface process in street canyon.
- Building-street layout affects urban surface heat budget, enhancing heat capacity and vertical mixing, verified by observation.
- Details of urban street canyon improve simulating environmental and meteorological variations, especially in winter night.

GRAPHICAL ABSTRACT
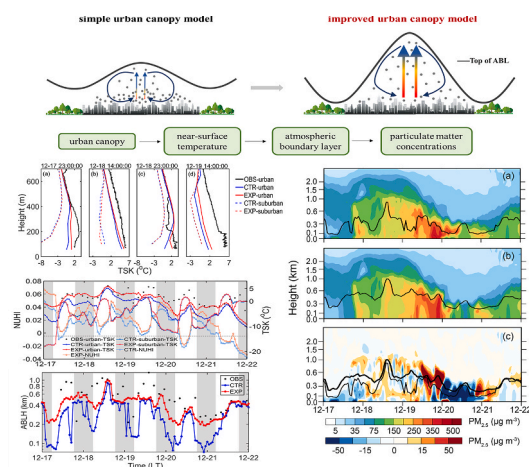
ARTICLE INFO

ABSTRACT

Urban heat island effect and local atmospheric boundary layer circulation caused by urbanization are important factors affecting the transport and spatial and temporal distribution of atmospheric particulate matter in cities and surrounding areas. To analyze the local atmospheric circulation and its influence on the temporal and spatial characteristics of PM$_{2.5}$ concentration over the Central Liaoning Urban Agglomeration, a heavy haze process was selected. The atmospheric chemistry model WRF-Chem was applied for numerical simulations with sensitivity experiments of urban canopy physical processes. The experiment case (EXP) was set up by coupling an improved urban canopy model with WRF-Chem, in which more details of inhomogeneous wind and diffusion in the complexed street canyon were fully and reasonably considered. Compared with the control case (CTR) by the original WRF-Chem, the deviation of the simulated and observed near-surface temperature and atmospheric boundary layer height was significantly improved in EXP: the error during the daytime was reduced from -1.30% and -48.39% in CTR to -0.78% and -33.68% in EXP, respectively, while during the nighttime it was reduced from -1.15% and -48.98% to 0.05% and -24.42%. The simulation accuracy of the near-surface PM$_{2.5}$

---

* Corresponding author.
  E-mail address: liuzhenxin@nuist.edu.cn (Z. Liu).

concentration in EXP was also significantly higher: the deviation during the daytime was 18.24% in CTR and 3.28% in EXP, while it was reduced from 40.69% in CTR to 28.88% in EXP during the nighttime. Thus, the EXP improved significantly in meteorological simulation during the nighttime, and then particulate matter concentrations in EXP during the nighttime were obviously improved. This study shows that improving the wind profiles and diffusion mechanism in urban canopy schemes in the air quality model can effectively improve the simulation ability of the model on the transport and diffusion processes of atmospheric pollutants in cities and surrounding areas, thus improving the simulation ability of urban near-surface air pollution concentration.

1. Introduction

In recent years, China has experienced a rapid and large-scale urbanization process, and many natural vegetation underlying surfaces were converted into artificial constructions (Li et al., 2016; Yang et al., 2020a). The process of urbanization increases the difference in the concentrations of particulate matter between urban and suburban areas (Crutzen, 2004; Zhang et al., 2022). Studies have shown that the concentration of $PM_{2.5}$ rose by 1.25 μg m^{-3} for every 1% increase in the urbanization rate (which reflects the proportion of urban area) of China (Wang and Fang, 2016). Approximately two-thirds of Chinese cities have the phenomenon of Urban Haze Island, with the criterion of over 2 μg m^{-3} difference in $PM_{2.5}$ concentration between the city center and the suburban area 30 km away from the city (Zhu et al., 2020). And most of the population is exposed to the atmosphere with the concentration of particulate matter greater than the national secondary standard for a long time (Li et al., 2020d).

Further research shows that the correlation between urbanization and air quality index is greater in northern China than in southern China, especially in autumn and winter in many areas (Fang et al., 2015). Northeast China is the earliest industrialized and urbanized region in China. Meanwhile, the concentration of $PM_{2.5}$ in the region increased at a rate of about 4 μg m^{-3} per year from 1979 to 2015 (Shi et al., 2019; Zhang et al., 2015), with the highest concentration in winter during the year (Li et al., 2020a, 2020c). In early November 2015, the most severe haze pollution event in history occurred in Shenyang, one of the most important cities in Northeast China, with $PM_{2.5}$ concentration reached 848 μg m^{-3} (Fu and Chen, 2017). After that, air pollution events with a peak concentration of more than 200 μg m^{-3} for $PM_{2.5}$ occurred almost every winter (Li et al., 2019a, 2019b; Liu et al., 2021). In another major city in Northeast China, Harbin, the monthly average concentration of $PM_{2.5}$ also reached 150 μg m^{-3} in January 2020 (Cheng et al., 2022). The industry-dominated economy and the severe winter weather led to relatively higher $PM_{2.5}$ concentration in these cities during the winter months (Fan et al., 2020; Li et al., 2016; Meng et al., 2021b; Yang et al., 2020b; Zhang et al., 2017). The transport of air pollutant occurred frequently between Harbin, Changchun and Shenyang made the air pollution situations even worse (Li et al., 2020a, 2020c). In addition, the transport from Mongolia, southern Russia, northwestern Inner Mongolia, eastern Hebei, and eastern Jiangsu (Ma et al., 2021a, 2021b) greatly contributed to the $PM_{2.5}$ concentration in Northeast China (Li et al., 2020b). In an air pollution event in January 2019, the contribution of transport from the Beijing-Tianjin-Hebei region to the $PM_{2.5}$ concentration in Shenyang reached 60% (Zhao et al., 2020).

The convection and vertical turbulent transport have an important influence on the concentration of air pollutants from near-surface emissions and regional transport (Cai et al., 2017; Lv et al., 2020). Atmospheric boundary layer height (ABLH) and near-ground wind speed over urban areas are the key factors to evaluate the intensity of the influence above (Luan et al., 2018; Su et al., 2018; Yin et al., 2019). Urban ABLH and urban near-surface wind speed, influenced by the characteristics of urban land surface processing (Daniel et al., 2019; He et al., 2020; Ma et al., 2022; Rafael et al., 2017; Yang et al., 2019), are significantly different from those over the surrounding suburban areas (Gu et al., 2011; He et al., 2018). Thus, the effect of urban heat island circulation (UHIC), which is caused by the thermal and dynamic

differences between the urban and suburban areas, ultimately impacts the accumulation and transport of near-surface air pollutants in urban areas. Many studies have shown that the diurnal and seasonal characteristics of UHIC vary in different areas (Kim et al., 2021; Liu et al., 2020; Tam et al., 2015). In Northeast China, which is concerned in this study, the UHIC effect is stronger in winter and at night compared to other regions, which may be due to the relatively stronger human activities in these periods (Zhou et al., 2023).

Therefore, it is crucial to apply an urban canopy model that fully considers the land surface characteristics of urban built-up canopy and its effect on the land surface processing in simulations of urban atmospheric environment. However, most of the current applied urban modules in the mesoscale air quality models, either set constants to parameterize the urban land surface characteristics, such as surface albedo and aerodynamic roughness (Myrup, 1969), or established the simple mathematical models of urban buildings and streets to solve the energy balance equations of the building roofs, walls and road surfaces, respectively (e.g., Town Energy Budget (TEB) (Masson, 2000), Urban Canopy Model (UCM) (Kusaka et al., 2001; Ryu et al., 2011)). And then the environmental meteorological variables such as air temperature, turbulent kinetic energy, wind speed, wind direction and air pollutant concentration and their diurnal variations in urban street valleys were obtained (Cheng and Porte-Agel, 2021; Kusaka et al., 2001; Lee and Park, 2008; Wang et al., 2021a; Yang et al., 2015).

However, more improvement is still needed in the simulation of the near-surface air pollutant concentrations and related vertical turbulent transport in and around cities, especially during the nighttime or in the winter, when the simulated vertical diffusion intensity of turbulence tends to always be on the low side in atmospheric environment simulation (Chu et al., 2019; Garuma, 2018; Huang et al., 2019; Meng et al., 2021a; Sun et al., 2021; Yang et al., 2015), which leads to the deviation of the model simulated temporal and spatial distribution of atmospheric pollutant concentration (Wang et al., 2021b).

Therefore, to preferably study the process of air pollution events at night during winter, the Multi-Scale Urban Canopy Model (MSUCM) (Liu, 2013) was coupled with the WRF-Chem as the model base for this study. The MSUCM model takes into account more details of the inhomogeneity of wind and turbulence in the street canyon over the urban areas (Liu et al., 2023), which makes it better to simulate the nocturnal urban land surface process.

The Central Liaoning Urban Agglomeration (CLUA) concerned in this study is one of the most important urban agglomerations in Northeast China and it developed the earliest in the process of industrialization and urbanization in China. At present, it is dominated by heavy industry and has a high urbanization rate. The huge anthropogenic heat emissions cause significant thermal differences between the urban and surrounding suburban areas in CLUA, especially in winter and at night (Zhang et al., 2020; Zhao et al., 2013). Therefore, a typical heavy haze process in CLUA in the winter of 2016 was selected for numerical simulations and sensitivity experiments and compared with the observation. We mainly focused on the spatiotemporal characteristics of $PM_{2.5}$ concentrations, as well as the vertical temperature profiles and mixing heights associated with particle matter transport. Particular attention was paid to how vertical mixing near the urban surface at night affected temporal variations in particulate matter concentrations.

2. Data, methods and model

2.1. Design of numerical experiments

In this study, the WRF-Chem model 3.9.1.1 (https://ruc.noaa.gov/wrf/wrf-chem/) was applied to simulate a heavy haze event in CLUA on December 16th −21st, 2016. The numerical sensitivity experiments of urban canopy physical process scheme were set up. MSUCM was applied in the experiment case (EXP) as the urban canopy model, while in the control case (CTR), the Single-Layer Urban Canopy Model (SLUCM) (Kusaka et al., 2001) was called. The other schemes of physical and chemical parameterization for both the EXP and CTR cases were kept the same, as shown in Table 1. The simulated meteorological variables (e.g., near-surface temperature (TSK), ABLH) and pollutant concentration variables (e.g., PM$_{2.5}$ and PM$_{10}$) in the two cases were compared, and the observations were also used for validation. Finally, the impact of surface energy budget and urban heat island (UHI) effect on the physical mechanisms of urban local air pollution diffusion and transport processes was analyzed.

The CLUA is located in the central Liaoning Plain, where Shenyang, Benxi, Anshan, Fushun and several other industrial cities are included. Hilly terrain lies on the eastern and northern sides of the CLUA, while on the southeast side is mainly river floodplain. As shown in Fig. 1, the center of the simulation area was set at 41°5′N, 123°2′E, and one 32 km parent domain and two double nested domains of 8 km and 2 km resolution were set-up while two-way nesting was applied. Final Operational Global Analysis (FNL) by the National Center for Atmospheric Research (NCAR) was used as the initial global meteorological field with a resolution of 1° × 1°. The simulation period was set to be December 13th - 21st, 2016. The first four days were used for spin-up, and the simulation results during December 17th - 21st, 2016 were selected for analysis.

2.2. Main different physical processing in MSUCM and SLUCM

In this study, the SLUCM and MSUCM were coupled to WRF-Chem for sensitivity experiments of the urban land surface process. The main different features of SLUCM and MSUCM are as follows:

The SLUCM, based on the homogeneity assumption, utilizes the classic exponential-logarithmic profile to derive the average wind field distribution characteristics at urban grid points as shown in Fig. 2. However, in reality, due to the influence of inhomogeneous distributed buildings, the wind field at various grid points in urban street canyons is horizontally non-uniform. The MSUCM accounts for the spatial inhomogeneity of wind and turbulence at scales ranging from 10 m to 1 km within street canyons. It introduces new wind profiles at 6 different presentive spots on the leeward and windward within the canyon (Liu et al., 2023). As shown in Fig. 2b and c, the wind speed near and under the average height of the urban street canyon simulated by MSUCM is

Table 1
The parameterization schemes list in the WRF-Chem sensitivity simulations in this study. The main difference between EXP and CTR is in bold.

| Parameterization scheme	CTR	EXP
Urban Canopy Model	**SLUCM (Kusaka et al., 2001)**	**MSUCM**
Gas phase chemistry	RADM2 (Stockwell et al., 1990)	
Microphysics	Lin (Lin et al., 1983; Rutledge and Hobbs, 1984)	
Cumulus physics	Grell 3D	
Longwave radiation	RRTMG	
Short wave radiation	RRTMG	
Surface Layer	MM5	
Planetary boundary layer	MYNN 2.5 level TKE (Nakanishi and Niino, 2009)	
Anthropogenic emissions	MEIC	
Biogenic emissions	Megan	
Biomass burning emissions	FINN	
Aerosol	RADM2/SORGAM (Schell et al., 2001)	
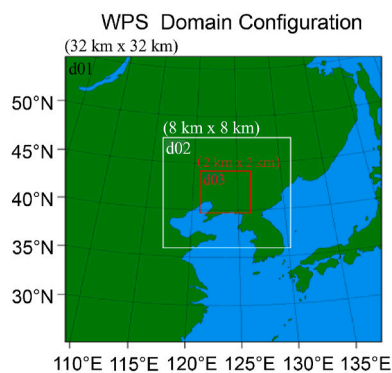
Fig. 1. Domains setting in model simulation for this study.

lower than that by SLUCM, causing the sensitive heat flux in the street canyon more consistent with the observation (Offerle et al., 2007).

2.3. Observational data

In this study, the observations of TSK, ABLH, PM$_{2.5}$ and PM$_{10}$ concentrations in Shenyang are used for model validation. A boundary layer observational project was conducted from 11:00 Local Time (LT) on December 17th to 14:00 LT on December 23rd, 2016 in Baitapu Town (41.6841°N, 123.4160°E), which is located 8 km south of the central urban region of Shenyang. The Model Chuangzhi Tan Kong-1 (CZTK-1) sounding system, developed by the Institute of Atmospheric Physics of the Chinese Academy of Sciences, was used to measure the vertical distributions of wind speed (WS), wind direction (WD), air temperature (T_a), and relative humidity (RH). The detective resolutions are 0.1 m s^{-1}, 0.1°, 0.1 °C, and 0.1%, respectively, as shown in Table S1. Sounding balloons were released at an open balcony of a low building (height <3 m) eight times per day at 02:00, 05:00, 08:00, 11:00, 14:00, 17:00, 20:00, and 23:00 LT, and a total of 50 groups of profile data were obtained. The ABLH was estimated based on the vertical temperature profile observation by the bulk Richardson number (Ri) method, as shown in eq. (1). Moreover, hourly mean mass concentrations of PM$_{2.5}$ and PM$_{10}$ in Shenyang were obtained from the Liaoning real-time air quality publishing system (http://211.137.19.74:8089/). More detailed information about the observations, which is not important in this study, can be found in Li et al. (2018).

2.4. Determination of the ABLH

In this study, the ABLH from observation is determined by the bulk Richardson number (Ri) method (Vogelezang and Holtslag, 1996) based on the observed vertical profiles of wind speed and potential temperature.

$$Ri(z) = \frac{\left(\frac{g}{\theta_{vs}}\right)(\theta_{vz} - \theta_{vs})(z - z_s)}{(u_z - u_s)^2 + (v_z - v_s)^2 + bu_*^2} \tag{eq. 1}$$

where z and s represent the height above the ground and the surface, respectively. g is the acceleration due to gravity, θv is the virtual potential temperature, u and v are the components of wind speed, u_* is the surface friction velocity and b is a constant. Since bu_* is far less than wind shear, this term can be ignored. In this method, the ABLH is the lowest height at which Ri reaches a critical value. According to other research on ABLH (Guo et al., 2016; Huo et al., 2021), the critical value is set to 0.25 in this study.

The planetary boundary layer scheme used in two simulation cases is the MYNN 2.5 level TKE, a 1.5-order local closure scheme. It determines the ABLH based on the threshold of the turbulent kinetic energy (TKE), with the ABLH defined as the height where the TKE falls below a critical
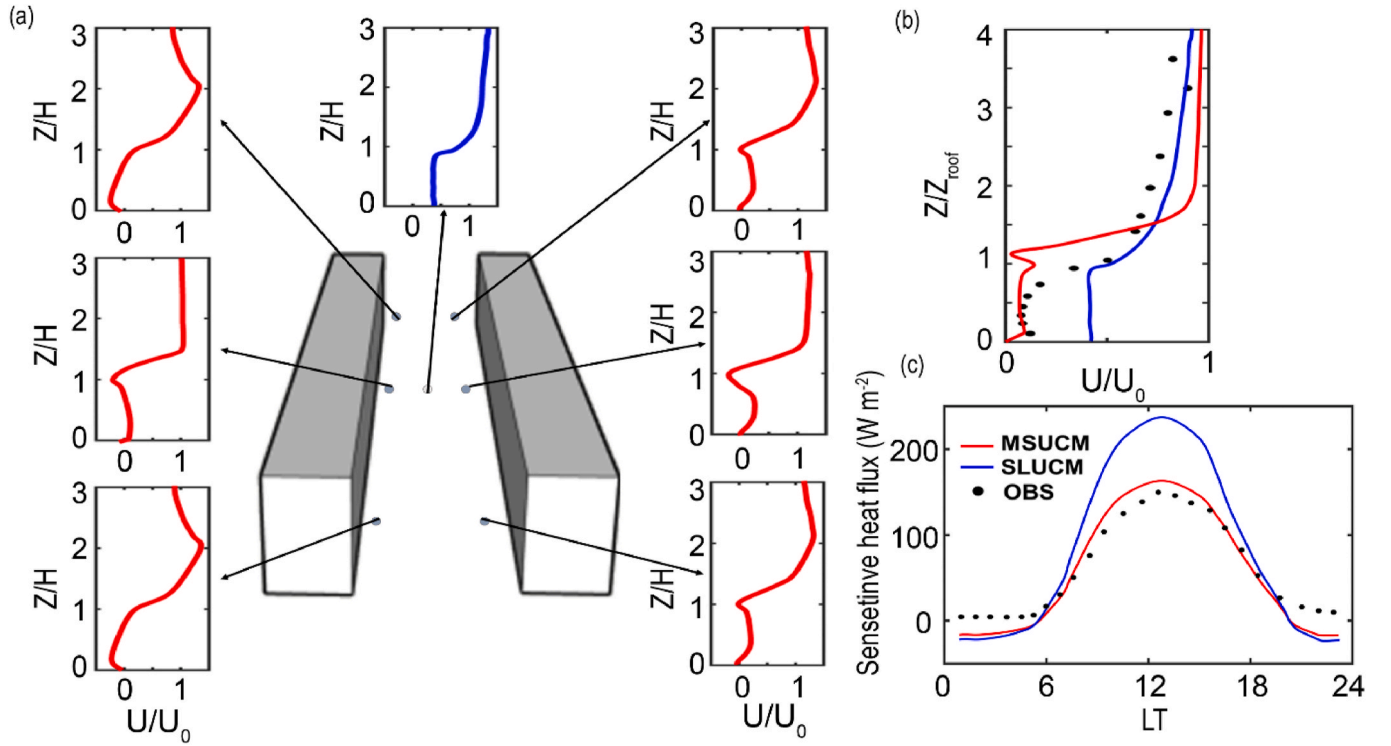
Fig. 2. (a) Wind profiles of the u component in the urban street canyon in MSUCM (red line) at different positions and SLUCM (blue line) from Liu et al. (2023). (b) Overall averaged vertical wind profiles from MSUCM (red line), SLUCM (blue line) and observations (black dots) from Liu et al. (2023). (c) Daily variation of sensible heat flux simulated by MSUCM and SLUCM and observed (OBS) by Offerle et al. (2007).

value of 1.0×10^{-6} m^2 s^{-2} (Banks et al., 2016; De Lange et al., 2021).

2.5. Definition of NUHI

In this study, normalized urban heat intensity (NUHI) is defined to characterize the urban heat island intensity. The formula is as follows:

$$NUHI = \frac{(TSK_{urban} - TSK_{suburban})}{TSK_{suburban}} \qquad \text{(eq. 2)}$$

where TSK_{urban} represents the mean value of TSK of urban areas, and $TSK_{suburban}$ represents the mean value of TSK of suburban areas other than urban areas in the simulation area.

2.6. Definition of AEC

In this study, atmospheric environmental capacity (AEC) is defined as the capacity to vertically diffuse air pollutants, determined by key local meteorological conditions such as atmospheric boundary layer height and near-surface wind speed. The formula is as follows:

$$AEC = ABLH * WS \qquad \text{(eq. 3)}$$

where WS and ABLH represent the wind speed and the atmospheric boundary layer height, respectively. In observation, the ABLH was obtained from the sounding system and calculated by eq. (1), while in simulation cases, it was calculated by averaging the simulated ABLH over the model grids representing the focused urban area.

2.7. Validation method

In this study, the following statistical indexes are applied to validate the simulation results in EXP and CTR cases. These are normalized mean bias (NMB), normalized mean error (NME), root mean square error (RMSE) and correlation coefficient (r), respectively. The definitions of

them are as follows:

$$NMB = \frac{\sum_{1}^{N} (S_i - O_i)}{\sum_{1}^{N} O_i} \times 100\% \qquad \text{(eq. 4)}$$

$$NME = \frac{\sum_{1}^{N} |S_i - O_i|}{\sum_{1}^{N} O_i} \times 100\% \qquad \text{(eq. 5)}$$

$$RMSE = \sqrt{\frac{\sum_{1}^{N} \left(\frac{S_i - O_i}{O_i}\right)^2}{N}} \qquad \text{(eq. 6)}$$

$$r = \frac{\sum (S_i - \overline{S}) \sum (O_i - \overline{O})}{\sqrt{\sum (S_i - \overline{S})^2 \sum (O_i - \overline{O})^2}} \qquad \text{(eq. 7)}$$

where S_i and O_i represent the simulated value and the observed value of a variable, respectively, and N indicates the number of the variable. $\overline{S}$ and $\overline{O}$ represent the mean value of the simulation and observation of a variable, respectively. In this study, TSK, ABLH, AEC, PM$_{2.5}$, and PM$_{10}$ were the main focus variables, and the simulations of these variables in both EXP and CTR cases were evaluated by the formula above. When the values of NMB, NME and RMSE are closer to 0, and the value of r is closer to 1, the better the modeling performance is.

$$t = \frac{\overline{X_1} - \overline{X_2}}{\sqrt{\frac{V_1^2}{n_1} + \frac{V_2^2}{n_2}}} \qquad \text{(eq. 8)}$$

where $\overline{X_1}$ and $\overline{X_2}$ are the mean value of the differences between two cases and observation, V_1^2 and V_2^2 are the variances of the differences be-

tween two cases and observation, and n_1 and n_2 indicate the number of a variable in two cases, respectively.

At the 95% confidence level, a two-sample Student's t-test was performed for all variables involved in this study in order to assess the statistical significance of the differences in deviations between the simulation results in each case and the observations. If the t-value exceeds the critical value, it means the significance test is passed, indicating a significant difference in deviations between the simulation results by EXP and CTR and the observations. Furthermore, if the NMB, NME, and RMSE values of EXP are closer to 0 compared to the CTR, it indicates that the simulation accuracy of these variables in EXP is significantly improved.

3. Results and discussion

3.1. Simulation and validation of TSK and TKE

Fig. 3 illustrates the time series of TSK and NUHI in the urban and surrounding suburban areas of CLUA in both simulation and observation (OBS). The black dots represent observed TSK in urban areas. Red dots and red triangles indicate simulated TSK in urban and suburban areas in the EXP case, respectively, while blue dots and blue triangles represent those in the CTR case. Orange and blue squares represent NUHI in the EXP and CTR cases, respectively. Shaded areas denote nighttime periods, and the white areas denote daytime periods. As shown in Fig. 3, the observed and simulated TSK in the study period showed obvious diurnal variation: lower during the nighttime while higher during the daytime. The TSK difference of urban areas between daytime and nighttime was about 7 °C. The values and duration variation in EXP were closer to OBS than those in CTR. Especially, the TSK in urban areas during the nighttime in CTR was obviously lower than OBS and more deviated than those in EXP, while two simulation cases show minor differences in simulating the TSK of suburban areas. In both CTR and EXP cases, the diurnal variation of TSK in suburbs was larger than that in urban areas. The maximum difference of TSK in suburbs between day and night reached more than 10 °C. And the TSK difference between urban and suburban areas during the nighttime was larger than that during the daytime.

In urban areas, the decline rate of TSK during the nighttime in EXP was significantly slower than that in suburbs and also in CTR. This slower cooling rate caused the TSK during the nighttime in urban areas

to be significantly higher in EXP than that in CTR and the suburbs, with a smaller difference of urban TSK between daytime and nighttime. As shown in Fig. 2c, the sensible heat fluxes in the urban street canyon in MSUCM, which were more consistent with the OBS, were lower than those in SLUCM throughout the day. During the nighttime, the TSK in the urban street canyon gradually decreased due to radiative cooling. The smaller flux in MSUCM slowed down the cooling rate, leading to higher TSK in EXP. During the daytime, solar radiation is the main heat source in the urban street canyon. Although the sensible heat fluxes in MSUCM were smaller than those in SLUCM, the increase of TSK from early morning began at a higher value due to the stronger heat storage effect at night. Therefore, it led to smaller TSK differences between the two cases during the daytime. This mechanism results in a smaller diurnal variation of TSK in urban areas in EXP than that in CTR, which is more consistent with OBS. Therefore, the simulation in EXP more accurately captures the energy balance processes within the urban street-valley canopy than those in CTR.

Fig. S1 is a scatter plot to evaluate the bias of simulated TSK in urban areas by EXP and CTR during the study period, where the X value of each scatter point stands for the observed TSK by OBS, while the Y value stands for the simulated values. The red dots represent EXP results and the blue dots represent CTR results. The red solid line and blue solid line represent the linear fitting lines for EXP and CTR cases, respectively. Thus, the closer the data point is to y = x (the black dotted line), the more consistent the simulation is with the OBS. Fig. S1a illustrates the data during the daytime, while Fig. S1b illustrates the data for nighttime. In the simulation cases discussed in this paper, daytime and nighttime mainly refer to the 08:00 to 20:00 and 20:00 to 08:00 LT each day, respectively. As shown in the figure, the simulation in EXP was slightly closer to OBS than CTR case during the daytime, while the performance of EXP case was obviously better than that of CTR case during the nighttime. It proves that the application of MSUCM improves the performance of WRF-Chem in urban land surface processes, especially during the nighttime. This conclusion is consistent with the analysis of Fig. 3.

The evaluation results of the deviation between the simulated and observed TSK in urban areas are summarized in Table 2. The statistical indicators NMB, RMSE, NME and *r* are used for the evaluation. The analysis methods have been introduced in Section 2.7 of this paper. NMB shows us the average deviation values between simulation and observation. NME indicates the normalized mean of absolute deviation. RMSE
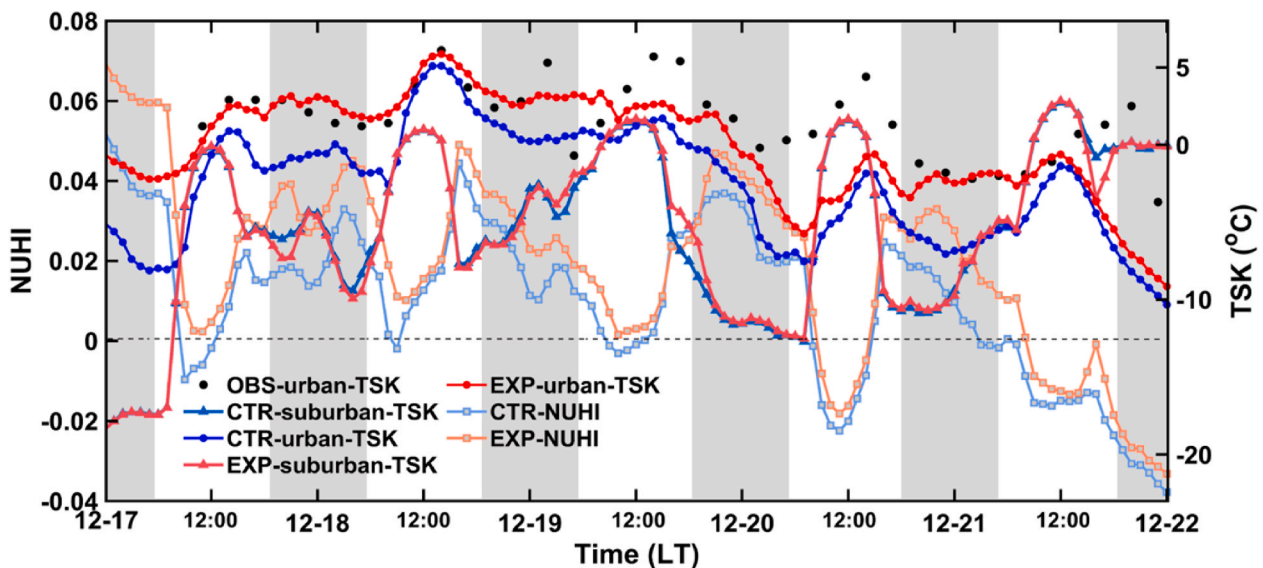

Fig. 3. Time series of TSK and NUHI in urban and suburban areas of CLUA. The black dots represent observed TSK in urban areas. Red dots and red triangles indicate simulated TSK in urban and suburban areas in the EXP case, respectively, while blue dots and blue triangles represent those in the CTR case. Orange and blue squares represent NUHI in the EXP and CTR cases, respectively. Shaded areas denote nighttime periods, and the white areas denote daytime periods.

Table 2

Simulation bias evaluation of key variables. The variables with better performance in EXP than in CTR and those pass the two-sample Student's t-test of significance are in bold.

Key variables	NMB (%)		NME (%)		RMSE		r	
	CTR	EXP	CTR	EXP	CTR	EXP	CTR	EXP
TSK (daytime)	−1.30	**−0.78**	1.30	**0.85**	0.02	**0.01**	0.67	0.65
TSK (nighttime)	−1.15	**0.05**	1.20	**0.38**	0.01	**0.00**	0.79	**0.80**
ABLH (daytime)	−48.39	−33.68	48.66	36.20	0.34	0.26	0.39	0.58
ABLH (nighttime)	−48.98	**−24.42**	48.98	**24.95**	0.38	**0.21**	0.50	**0.77**
PM$_{2.5}$ (daytime)	18.24	3.28	35.66	37.02	0.25	0.23	0.75	0.75
PM$_{2.5}$ (nighttime)	40.69	**28.88**	43.22	**32.82**	0.32	**0.24**	0.80	**0.86**
PM$_{10}$ (daytime)	−12.10	−23.24	29.45	34.36	0.21	0.23	0.65	0.68
PM$_{10}$ (nighttime)	7.96	**−1.20**	23.71	**18.57**	0.18	**0.13**	0.78	**0.84**
AEC (daytime)	−51.73	**−14.52**	51.76	**24.70**	0.30	**0.15**	0.77	**0.86**
AEC (nighttime)	−44.49	**7.38**	44.49	**24.21**	0.26	**0.16**	0.86	**0.88**

is the statistical variance of normalized deviation between simulation and observation, and the value r indicates the correlation between simulation and observation. The data illustrating better performance of EXP than those in CTR and also passing the two-sample Student's t-test of significance are in bold in the table. According to Table 2, the deviation of TSK between EXP case and OBS was generally smaller than that
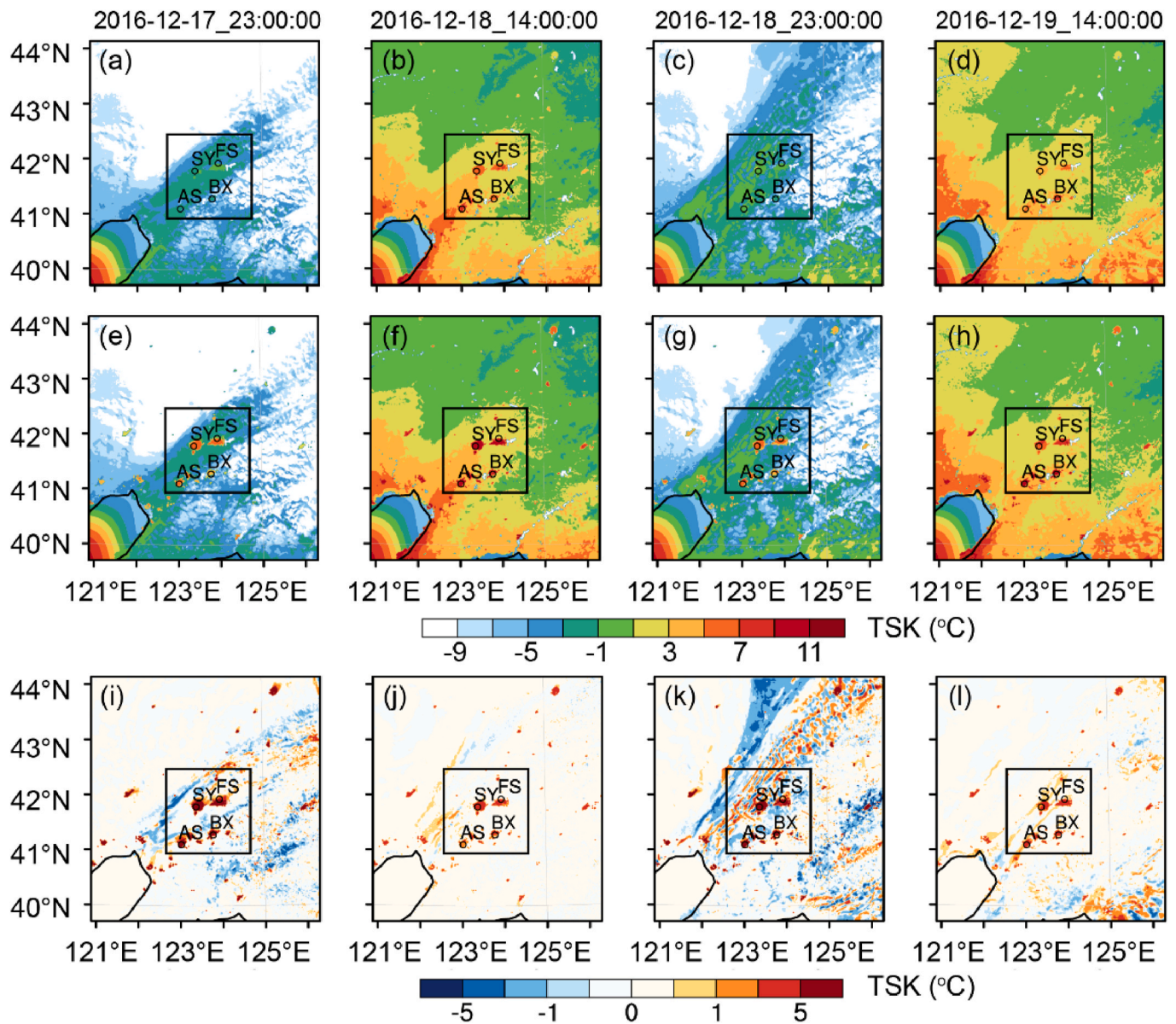

Fig. 4. Horizontal spatial distribution of TSK in (a–d) CTR case, (e–h) EXP case and (i–l) the difference between the two cases at four typical moments, where SY, FS, BX, AS represent Shenyang, Fushun, Benxi and Anshan, respectively. In i-l, the warm colors indicate that the simulated TSK in EXP is higher than that in CTR, while the cool colors indicate the opposite.

between CTR case and OBS. The trend was more obvious for the data during the nighttime. Meanwhile, the value *r* between TSK values by EXP and OBS was higher than that between CTR and OBS. It also proves that the MSUCM model has significantly improved the simulation of TSK.

Fig. 4 illustrates the horizontal spatial distribution of TSK in both CTR and EXP cases and the difference between the two cases at four typical moments during the study period. The black box shows the locations and spatial range of CLUA, and the black circles mark the locations of Shenyang (SY), Fushun (FS), Anshan (AS) and Benxi (BX), which are four of the most important industrial cities in CLUA. The 14:00 LT on December 18th and 19th are selected as the typical moments to represent the daytime, and the 23:00 LT on December 17th and 18th are selected to represent the nighttime, respectively. Temperature profiles by sounding experiments are available at these four typical moments for further comparison with the simulated temperature results. Fig. 4a–d and 4e–h represent the horizontal spatial distribution of TSK in CTR and EXP cases, respectively, and Fig. 4i–l shows the horizontal spatial distribution of TSK differences between the EXP case and CTR case. The warm colors indicate that the simulated TSK in EXP is higher than that in CTR, while the cool colors indicate the opposite. It can be seen from Fig. 4 that the TSK distribution in the whole region showed a trend of gradually increasing from the northeast to the southwest at about 14:00 LT during the daytime, and the difference between the highest and lowest TSK was about 10 °C. And the TSK was generally low at nighttime. However, the TSK of CLUA was higher than that over other places. The simulated horizontal spatial distribution of TSK in both cases illustrate the UHI effect in the main urban areas in the CLUA, e.g., Shenyang, Fushun, Anshan and Benxi: In CTR case, the TSK difference between the urban and suburban areas was about 2–6 °C at night and about 3–8 °C during the daytime. While in EXP case, the TSK difference between the urban and suburban areas during the nighttime and daytime reached 8–14 °C and 4–10 °C, respectively. These simulated results indicate the stronger UHI effect in EXP than those in CTR, and also the stronger UHI effect during the nighttime than the daytime.

The intensity of UHI is quantified by NUHI. As shown in Fig. 3, the diurnal variation characteristics of NUHI were similar in both EXP and CTR cases. The NUHI during the nighttime was stronger than that during the daytime. Moreover, the NUHI in EXP case was generally 0.01 or higher than that in CTR.

As shown in Fig. 4i–l, the differences between the EXP and CTR cases mainly concentrate in urban areas. The TSK in urban areas in EXP was significantly higher than that in CTR during both the daytime and nighttime, and the TSK of Shenyang, Fushun, Anshan, Benxi in EXP was consistently 3 °C or higher than that in CTR, especially during the nighttime. Combined with Fig. 3, it shows that MSUCM applied in EXP better simulates the nocturnal heat storage effect in the urban canopy layer, thus forming a larger TSK difference between the urban and suburban areas than that in CTR. Therefore, the intensity of UHI simulated by EXP was stronger.

In addition, the black line in the lower left corner of each subplot in Fig. 4a–h stands for the coastline of the Bohai Sea in China, and that the lower left side of the line is the sea surface. The sea surface temperature boundary condition from the NCEP FNL data was applied in the simulations, and a horizontal gradient of temperature occured as shown in the figures. After interpolation in the three nested grids, a reasonable diurnal variation of the surface temperature horizontal distribution over the sea and land surface was produced in simulations.

Fig. 5 shows the vertical profiles of the observed and simulated air temperature in two cases at the four typical moments. The black solid line represents the observed values, while the blue and red solid lines show the air temperature of the urban area in CTR and EXP cases, respectively. Additionally, the blue and red dashed lines represent the air temperature of the suburban area in CTR and EXP, respectively. It can be seen from Fig. 5 that the vertical lapse rate of urban temperature below 1 km altitude was relatively consistent during the daytime, which was approximately 8 °C km^{-1}. At 14:00 LT on December 18th and 19th, the vertical temperature lapse rate of urban area changed abruptly at approximately 1 km and 1.3 km, respectively. According to the calculation method of ABLH described in Section 2.4, it can be inferred that they were the ABLH at each moment. During the nighttime, the urban temperature decreased overall at different altitudes, with a more significant decrease near the ground. As a result, there was an obvious vertical thermal inversion layer near the urban ground at 23:00 LT on December 17th and 18th, respectively, which existed at about 100–200 m and 200–500 m, respectively. However, under the inversion layer, both
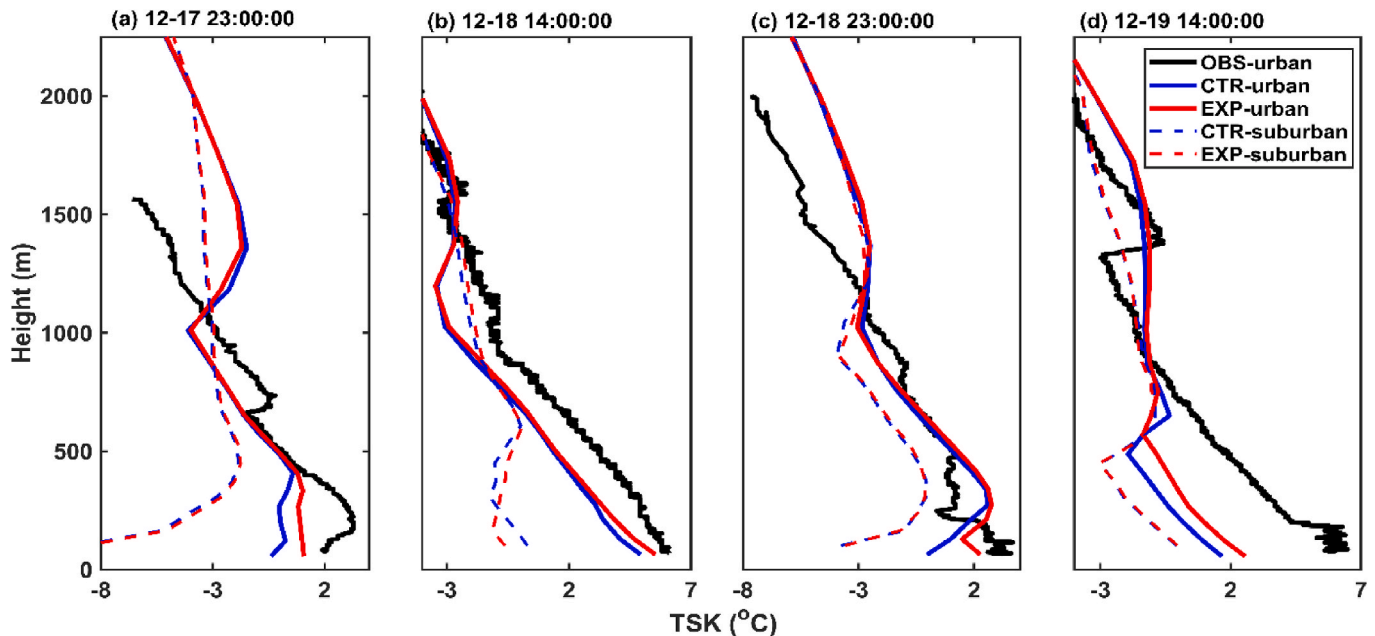

Fig. 5. Vertical temperature profiles in urban and suburban areas of CLUA at four typical moments. The black solid line represents the observed temperature in urban areas. The red solid line and the red dashed line are the simulated temperature in urban and suburban areas in CLUA in EXP case, respectively; the blue solid line and the blue dashed line are the simulated temperature in CTR case, respectively.

Fig. 5a and c showed the presence of a thin but distinct thermodynamic instability layer near the urban surface, which existed near the urban surface and about 250 m above the ground, respectively.

The simulated temperature profiles of urban area both in EXP and CTR cases at the four typical moments were in good agreement with the OBS. The unstable layer developed higher during the daytime, and the ABLH was also higher, while the temperature decreased overall at all altitudes during the nighttime, resulting in the profile moving to the left. And at the same time, an inversion layer occurred near the ground in urban areas. However, the simulated TSK near the ground (such as below 200 m) in EXP was closer to the OBS at the four typical moments than that in CTR. At the same time, the simulated temperature profiles in EXP case clearly indicated the presence of a near-surface unstable layer under the inversion layer at the two typical nocturnal moments, consistent with the observed urban characteristics. On December 17th, the near-surface unstable layer was located below 400 m in EXP case, and its vertical temperature lapse rate was significantly higher than that in CTR case, thus indicating stronger instability in EXP case. On December 18th, the near-surface unstable layer in EXP case only existed under the altitude of 100 m, but the intensity was stronger, and it was obviously different from the strong inversion layer developing from 0 m above the ground in CTR case. Therefore, the simulated temperature profiles in EXP case had a better agreement with the observation. While, apart from 14:00 LT on December 18th, there were no significant differences in the simulated temperature profiles of the suburban area from near the surface to around 2 km altitude between the two cases, and there was no presence of a near-surface unstable layer in the suburban area during the nighttime.

Both the OBS and simulation in EXP case showed similar thermally unstable layers under a certain height in the urban area, which did not exist over the urban area in CTR, and over the suburban area in both CTR and EXP during the nighttime. It shows the better performance of EXP at simulating the UHI effect during the nighttime.

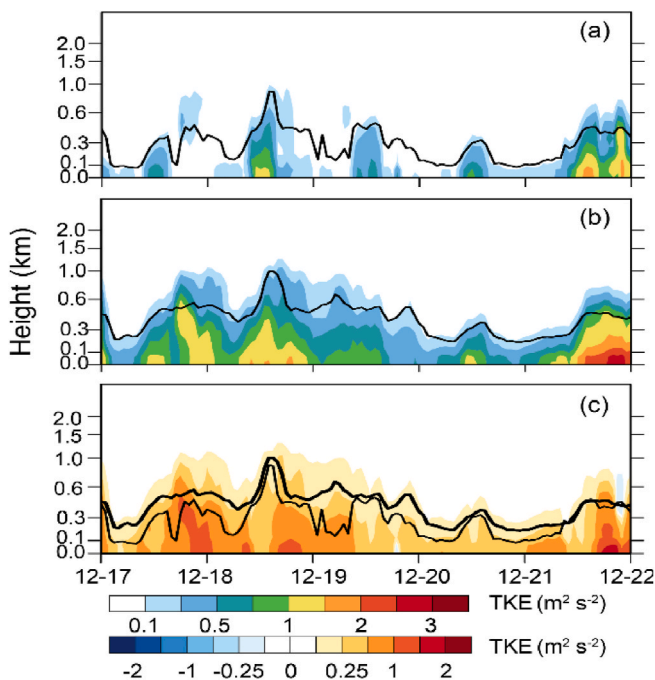The vertical temperature distribution is a key factor influencing the

atmospheric turbulence, and TKE represents the intensity of atmospheric turbulence. Fig. 6 shows the time series of vertical profiles of simulated TKE profiles in urban areas of CLUA in two cases. Fig. 6a represents the TKE in CTR, while Fig. 6b shows the TKE in EXP case. The black solid line shows the simulated ABLH in each case. Fig. 6c shows the difference between two cases, where warm colors indicate higher TKE in EXP and cool colors indicate the opposite. The thinner and thicker black lines represent the ABLH in CTR case and EXP case, respectively. In the two simulation cases, TKE gradually decreased from the surface to higher altitudes. In CTR, the near-surface TKE was mostly maintained at about 0.5 m^2 s^{-2}, while in EXP, it was generally between 0.9 and 1.5 m^2 s^{-2}, and the TKE difference between the two simulation cases could reach 1.5 m^2 s^{-2}. Figs. 3–5 indicate that the EXP had higher near-surface temperatures in urban areas, thus forming a stronger thermally unstable layer near the surface. This unstable temperature stratification will promote the generation of near-surface atmospheric turbulence. Therefore, the TKE in Fig. 6c was always positive, indicating that it was always higher in EXP than in CTR, and this difference was more obvious near the surface. In addition, the spatial and temporal distribution of TKE was in good agreement with that of ABLH. The boundary layer scheme used in this study calculates ABLH by finding the height at which TKE drops to the threshold as described in Section 2.4. Therefore, the higher the vertical distribution of TKE, the higher the ABLH. The detailed analysis of the temporal and spatial distribution characteristics of ABLH is shown in Section 3.2.

3.2. Simulation and validation of ABLH and AEC

Fig. 7 shows the time series of ABLH of urban areas in Shenyang in both simulation and OBS. The black dot represents the observed ABLH, and the red and blue solid lines are the simulated ABLH in EXP and CTR cases, respectively. The shadowed parts on the figure represent the nighttime periods, and the white parts are the daytime periods. It can be seen from Fig. 7 that the observed ABLH had a regular diurnal variation. Specifically, ABLH was relatively low during the nighttime, always staying below 600 m, and gradually increased from the morning and reached its peak in the afternoon, and the peak value could reach 1 km. Then, it decreased again around the evening. From December 20th, a warm advection system occurred in the upper layer of Shenyang, and the temperature inversion in the middle and upper layer was strengthened, which resulted in the ABLH decreasing by more than 300 m from December 17th to December 19th (Li et al., 2018). Both EXP and CTR cases well simulated the diurnal variation of ABLH during the study period. However, the simulated ABLH in CTR was significantly lower than the OBS during the whole day, especially during the nighttime. During the daytime, the ABLH in EXP was approximately 50–100 m higher than that in CTR, while during the nighttime, the ABLH in EXP was over 100 m in average higher than that in CTR and sometimes even could be more than 300 m higher than that in CTR. Therefore, the diurnal variation characteristics and numerical accuracy of urban ABLH in EXP case were significantly closer to OBS than those in CTR case, and the improvement at night was greater than that during the daytime. It has been illustrated in Section 3.1 that the temperature difference between urban and suburban areas in EXP was consistently stronger than that in CTR and was more significant at night than during the daytime. As a result, there was a stronger UHIC in EXP, which was manifested by higher near-surface mixing height and ABLH in urban areas. And from the perspective of circulation, the UHI simulated in EXP also showed a stronger characteristic during the nighttime than that during the daytime.

The scatter plot in Fig. S2 is the validation of simulated ABLH of urban areas in EXP and CTR by OBS. The results for daytime and nighttime are shown in Figs. S2a and b, respectively. The simulated ABLH in EXP was more coincident with the OBS during both the daytime and nighttime. The correlation coefficients (*r*-value) of simulating and OBS were 0.77 for EXP and 0.50 for CTR during the nighttime. During

Fig. 6. Time series of the vertical profiles of simulated TKE in urban areas of CLUA in (a) CTR case, (b) EXP case and (c) the difference of two cases. The black solid lines in (a) and (b) show the simulated ABLH in each case. In (c), warm colors indicate higher TKE in EXP and cool colors indicate the opposite. The thinner and thicker black lines represent the ABLH in CTR case and EXP case, respectively.
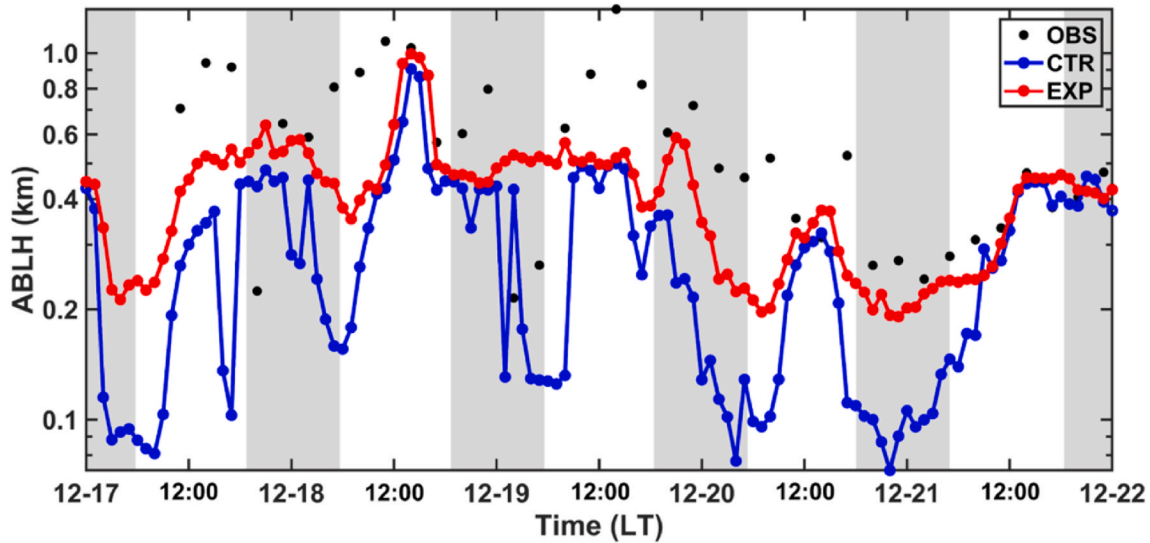
Fig. 7. Time series of ABLH in urban areas of CLUA. The black dots represent observed ABLH, while the red and blue solid lines indicate simulated ABLH in the EXP and CTR cases, respectively. Shaded areas denote nighttime periods, and white areas denote daytime periods.

the daytime, the *r*-value for EXP was 0.58 and only 0.39 for CTR. The rate of fitting line for EXP was also closer to y = x than those for CTR: during the daytime, it was 0.31 (EXP) to 0.24 (CTR), while 0.71 (EXP) to 0.47 (CTR). These results illustrate a significant underestimation of ABLH in both EXP and CTR. But the simulating ABLH in EXP was much improved and more coincident with those in OBS, especially during the nighttime. All of the statistical results summarized in Table 2 prove that the ABLH results simulated in EXP were obviously more consistent with the OBS, and the simulation deviation at night was significantly smaller than that during the daytime. The NMB, NME and RMSE of EXP during the nighttime were only about 50% of the corresponding indicators of CTR, proving that the MSUCM model has significantly improved the simulation of ABLH.

Fig. 8 illustrates the horizontal spatial distribution of ABLH at the four typical moments (the same as Fig. 4), including the horizontal spatial distribution in CTR case (Fig. 8a–d) and in EXP case (Fig. 8e–g) and the difference between the two cases (Fig. 8i–l). The black box provides the location and spatial range of CLUA. As shown in Fig. 8, the ABLH was affected by the terrain during the daytime. Therefore, the ABLH of CLUA and its southwest direction (e.g., the downwind direction during this period) was significantly higher than that in other areas, reaching 650 m and above. During the nighttime period, the ABLH in CLUA was generally low, with a maximum value of about 450–500 m. Under the influence of UHI effect, the ABLH of urban areas was higher than that of the surrounding suburban areas in two cases. In CTR case, the difference in ABLH between the urban and suburban areas was 100–200 m during the daytime and 100 m during the nighttime, while in EXP case, the difference in ABLH between the urban and suburban areas was approximately 200–300 m during the daytime and 150–250 m at night. It can be seen that the difference in ABLH between the urban and suburban areas in EXP was greater. As shown in the difference in horizontal spatial distribution of ABLH, the ABLH of urban areas in EXP case was about 100 m higher than that in CTR case during the daytime and significantly increased by 150–200 m at night, so the difference in urban ABLH simulated by the two cases was more significant during the nighttime. However, the difference in distribution also showed that the simulated ABLH of the surrounding areas around the urban areas in EXP case was 100–150 m lower than that in CTR case.

While a higher ABLH was generated over the urban area by MSUCM, a reduction of ABLH in surrounding areas was found. Then the horizontal distribution of the vertical mixing height and environmental capacity of pollutants in and around the urban areas in EXP were also

different from the CTR.

Wind speed and the atmospheric boundary layer are important meteorological factors influencing the transport and vertical mixing of local air pollutants, both of which significantly impact the spatiotemporal distribution of air pollutants. The AEC defined in this study effectively reflects the spatiotemporal distribution characteristics of local atmospheric environmental capacity and atmospheric vertical mixing ability, as determined by the combined effects of WS and ABLH. Fig. 9 is the time series of AEC in urban areas of CLUA, showing a diurnal pattern with higher values during the daytime and lower values at nighttime. The simulated AEC in EXP was significantly higher than that in CTR, with both the values and trends closer to the observation. Although the EXP still underestimated the AEC during the daytime, it showed significant improvements at nighttime. It was particularly obvious from the night of December 18th to the early morning of December 19th and the night of December 19th to the early morning of December 20th, when the EXP was not only more consistent with the observed AEC but also accurately captured its variation characteristics.

The scatter plots in Fig. S3 present the validation of the simulated AEC of urban areas in EXP and CTR by OBS. Figs. S3a and S3b show the results for daytime and nighttime, respectively. At night, the correlation coefficients (r-value) between the simulated AEC and OBS were 0.88 for EXP and 0.86 for the CTR. During the daytime, the correlation coefficient (r-value) for the EXP was 0.86, while it was only 0.77 for the CTR. The fitting line for the EXP was closer to y = x, especially at night. Most of the data points in both EXP and CTR were distributed below y = x, indicating that the two cases underestimated AEC, while the EXP occasionally overestimated AEC. As shown in Table 2, the NMB, NME, and RMSE of EXP in simulating AEC were lower than those of CTR during both daytime and nighttime, which further proves the simulated AEC in EXP was more consistent with the OBS. Therefore, the EXP significantly improves the simulation accuracy of AEC, indicating that the MSUCM model better captures the diurnal variation characteristics of near-surface atmospheric environmental capacity and vertical mixing capacity.

This section indicates that the MSUCM, applied in EXP, simulated higher ABLH and AEC in urban areas than SLUCM, which was more consistent with observations. These two metrological factors will affect the local diffusion and accumulation processes of atmospheric pollutants. And the mechanism is discussed in Section 3.3.
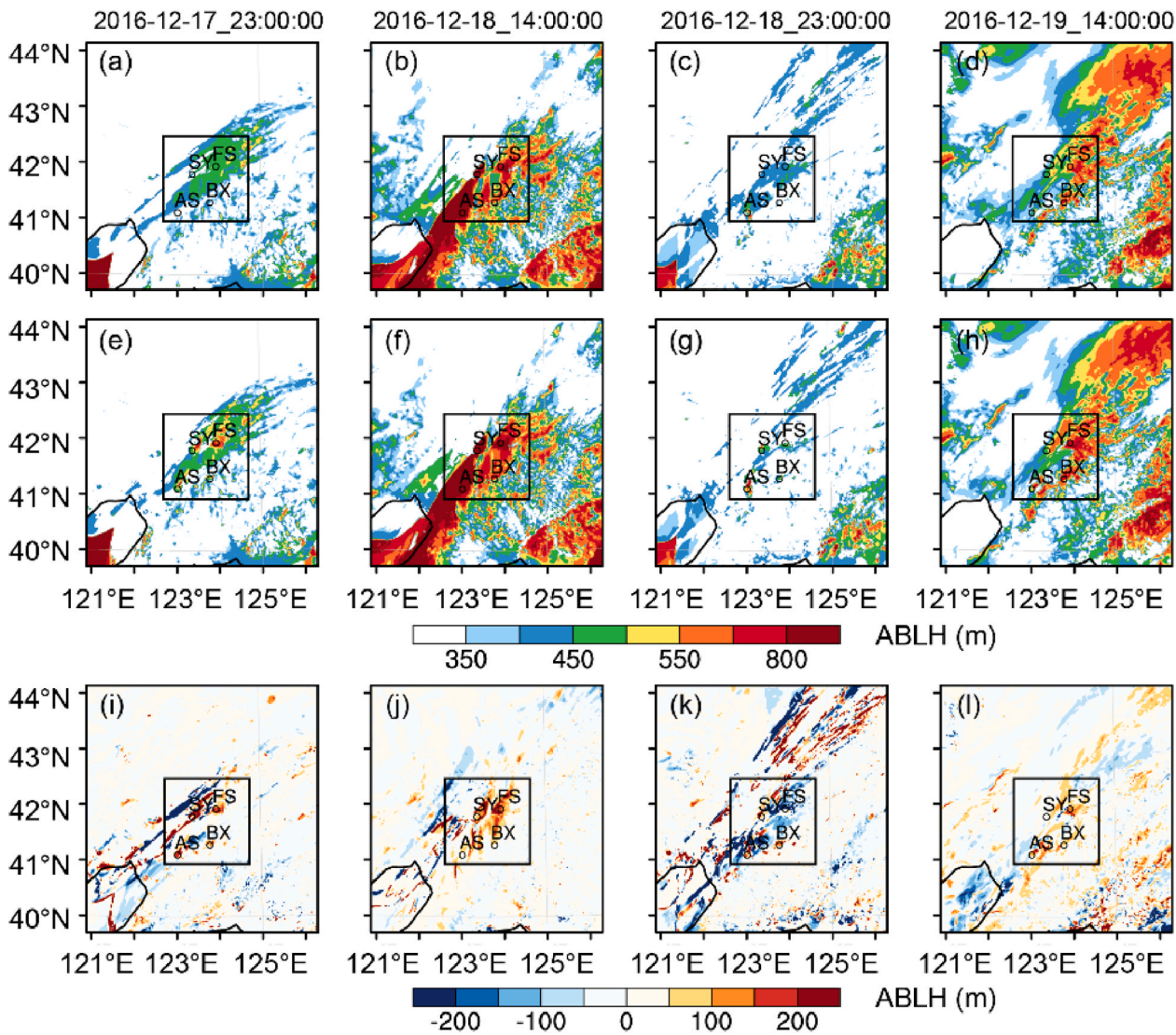
Fig. 8. Horizontal spatial distribution of ABLH in (a–d) CTR case, (e–h) EXP case and (i–l) the difference between the two cases at four typical moments, where SY, FS, BX, AS represent Shenyang, Fushun, Benxi and Anshan, respectively. In i-l, the warm colors indicate that the simulated ABLH in EXP is higher than that in CTR, while the cool colors indicate the opposite.
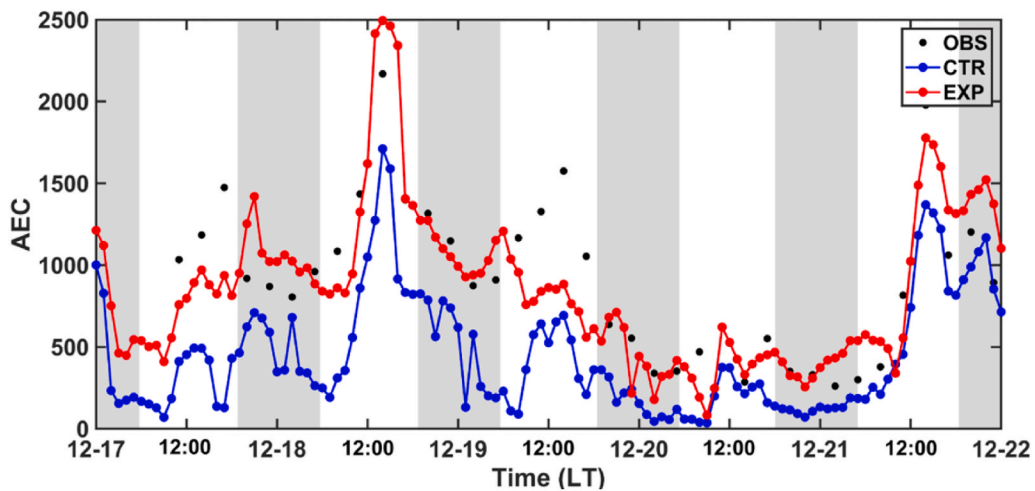

Fig. 9. Time series of AEC in urban areas of CLUA. The black dots represent observed AEC, while the red and blue solid lines indicate simulated AEC in the EXP and CTR cases, respectively. Shaded areas denote nighttime periods, and white areas denote daytime periods.

3.3. Simulation and validation of PM concentrations

Fig. 10 presents the time series of $PM_{2.5}$ and PM_{10} concentrations in urban areas of CLUA in simulation and OBS. The black solid line represents the observed concentration, while the blue and red solid lines separately represent the simulated concentration in CTR and EXP. The shadowed parts on the figure represent the nighttime periods, and the white parts are the daytime periods. As shown in Fig. 10, the observed $PM_{2.5}$ and PM_{10} concentrations show that the diurnal variation of them was regular and consistent, and the $PM_{2.5}$ concentration accounted for more than 60% of PM_{10} concentration. Therefore, this heavy atmospheric pollution event was a particulate matter pollution process dominated by $PM_{2.5}$. The daily average concentration of particulate matter began to increase from December 17th, and the hourly concentration reached its peak at the night of December 19th, with $PM_{2.5}$ concentration at about 280 μg m^{-3}, and the concentration of PM_{10} at about 380 μg m^{-3} at the same time. It can be seen from Fig. 10 that the diurnal variation of $PM_{2.5}$ and PM_{10} in EXP and CTR was in good agreement with the OBS, but both EXP and CTR cases overestimated $PM_{2.5}$ and PM_{10}. In comparison, the simulated $PM_{2.5}$ and PM_{10} concentrations in EXP case were generally lower than those in CTR case and the phenomenon was more pronounced during the nighttime. Therefore, the simulation by EXP was closer to OBS during the nighttime than daytime, although the simulated concentration in EXP case was still slightly higher than OBS during most nighttime periods.

Similar to Fig. S1, Fig. S4 is a scatter plot used to evaluate the simulated $PM_{2.5}$ and PM_{10} concentrations of urban areas in two cases. As shown in Fig. S4a, both CTR and EXP cases showed different degrees of underestimation when $PM_{2.5}$ concentration was less than 170 μg m^{-3}

during the daytime, while when $PM_{2.5}$ concentration was larger than 170 μg m^{-3} during the daytime, two cases tended to overpredict the concentration, and the deviation was generally greater than that of low concentration ($PM_{2.5}$ concentration was less than 170 μg m^{-3}). However, the $PM_{2.5}$ concentration was always overestimated in two cases at night. The correlation r shown in Table 2 between OBS and the simulated concentration by EXP was higher than in CTR, and the fitting line was closer to y = x, which proved that the simulation by EXP was more consistent with OBS. From Figs. S4c and d, it can be seen that the model performance of simulating PM_{10} was basically the same as simulating $PM_{2.5}$.

The statistical indicators in Table 2 further reflect the consistency between simulated particulate matter concentrations in two cases and OBS. As shown in the table, the deviation between the OBS and simulated particulate matter concentrations by EXP was generally smaller than that between the OBS and CTR and the improvement in simulating $PM_{2.5}$ and PM_{10} concentrations by EXP was better during the nighttime than the daytime. It was found that the deviation between the simulated TSK and ABLH in EXP case and OBS was only half of that between CTR and OBS, while in contrast, the simulated $PM_{2.5}$ and PM_{10} concentrations in EXP case were still relatively greatly deviated from OBS. The reason may be that the emission inventories used in the simulation process were uncertain, and it was difficult to ensure that they were consistent with the actual emission intensity and concentration of air pollutants.

Based on the improvement of important meteorological variables affecting the pollution process, such as TSK, ABLH and AEC, the spatial and temporal distribution characteristics of particulate matter concentrations in EXP were different from those in CTR. On the one hand, the
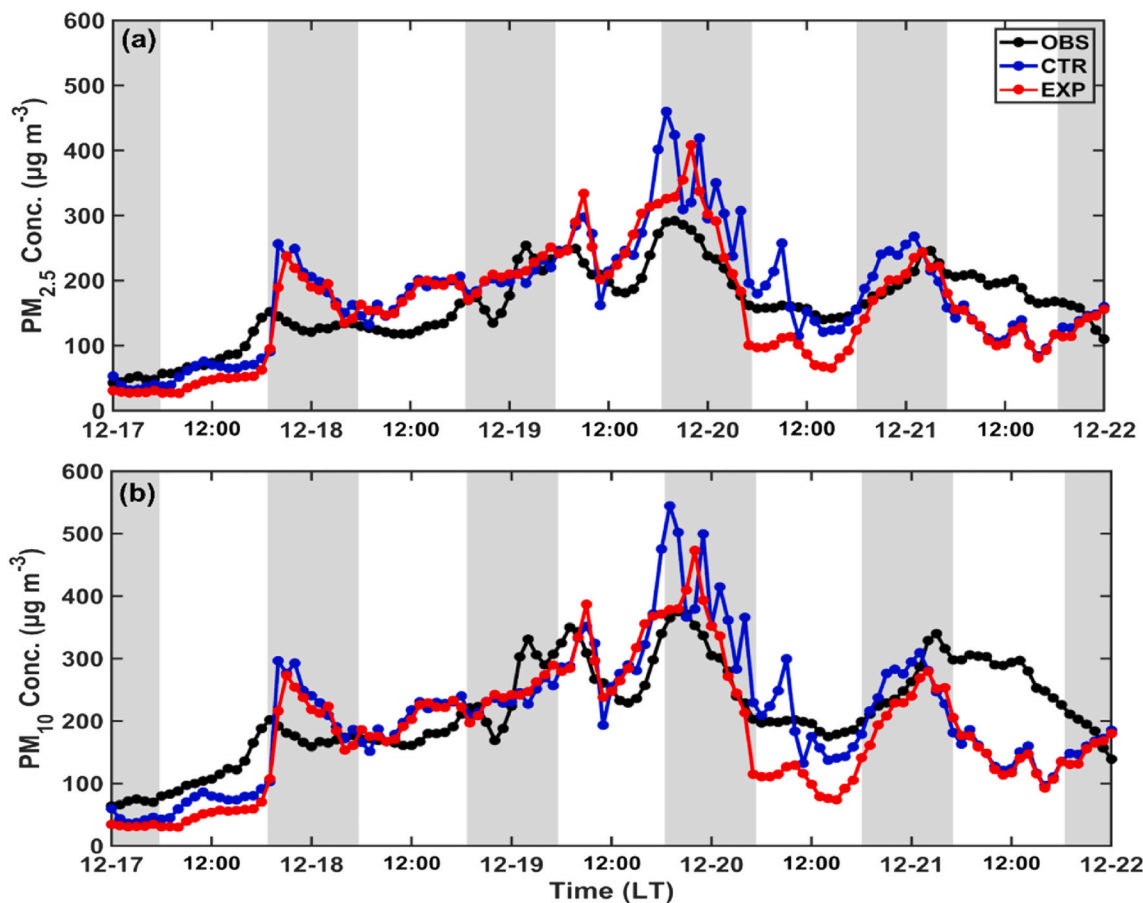

Fig. 10. Time series of (a) $PM_{2.5}$ concentration and (b) PM_{10} concentration in urban areas of CLUA. The black dots represent observed concentration, while the red and blue solid lines indicate simulated concentration in the EXP and CTR cases, respectively. Shaded areas denote nighttime periods, and white areas denote daytime periods.

EXP case effectively improved the model system problem of over-estimating concentrations near the ground, especially at night. On the other hand, the EXP case also improved the concentration characteristics of different episodes during the pollution event.

Fig. 11 are the time series of vertical profiles of simulated $PM_{2.5}$ and PM_{10} concentrations in urban areas of CLUA in two cases, respectively. Fig. 11a and d show the concentrations in CTR case; Fig. 11b and e show the concentrations in EXP case. The black solid line shows the simulated ABLH in each case. Fig. 11c and f present the difference between the two cases. The warm colors indicate that the concentration of particulate matter in EXP is higher than that in CTR, while the cold colors are the opposite. The thinner and thicker black solid lines represent the ABLH in CTR case and EXP case, respectively. As shown in Fig. 11, the process of the heavy haze event can be divided into three episodes according to the pollution characteristics, meteorological conditions and the difference between the two cases.

The first episode started from 0:00 LT on December 17th to 2:00 LT on December 18th. During this episode, there was cross-cities transport of particulate matter at high altitude, but the transport concentration was low, which had no obvious effect on the accumulation near the ground. Due to the higher ABLH and increased AEC in EXP case, the vertical mixing of pollutants in the atmospheric boundary layer was enhanced. As a result, the near-surface PM concentration was lower than that in the CTR case. The second episode was from 2:00 LT on December 18th to 1:00 LT on December 20th. The upper transport intensity of particulate matter increased, and the near-surface pollutant emission concentration became higher, so the pollutant accumulated rapidly below the atmospheric boundary layer. Due to the higher ABLH in EXP case, more pollutants had been transported and stored below the

atmospheric boundary layer. Therefore, from 100 m above the urban-surface, the particulate matter concentrations in EXP case were significantly higher than those in CTR case, especially on the night of December 19th, while higher ABLH also increased the vertical diffusion space in EXP case and caused particulate matter concentrations to decrease near the surface. However, as shown in Fig. 9, during the latter part of the second episode, AEC showed a gradual decline, which further promoted the development of the pollution event and led to a peak of PM concentration at the end of the second episode. The third episode, from 1:00 LT on December 20th to 24:00 LT on December 21st, ABLH was lower than the first two episodes, and the high-altitude transport and the near-surface pollutant emission concentration were significantly reduced. The ABLH in EXP case was still higher than that in CTR case, and the AEC showed a gradually increasing trend. This indicates that during this episode, the vertical mixing capacity and vertical mixing height in urban areas were increasing, especially in EXP. Therefore, the near-surface particulate matter concentrations in EXP were lower than those in CTR, which was similar to the first episode. This gradual enhancement of atmospheric vertical mixing capacity during the pollution event is an important meteorological condition for the end of the pollution event. Thus, by the end of the third episode, PM concentrations in both simulation cases significantly decreased.

The improvement in simulating $PM_{2.5}$ by EXP, which applied the MSUCM model, was mainly based on the improvement in simulating important meteorological conditions such as TSK and ABLH. The higher ABLH in EXP resulted in an increased AEC and then enhanced the vertical mixing of the near-surface pollutants than those in CTR. Therefore, the accumulation rate of pollutants in EXP was obviously slower than CTR.
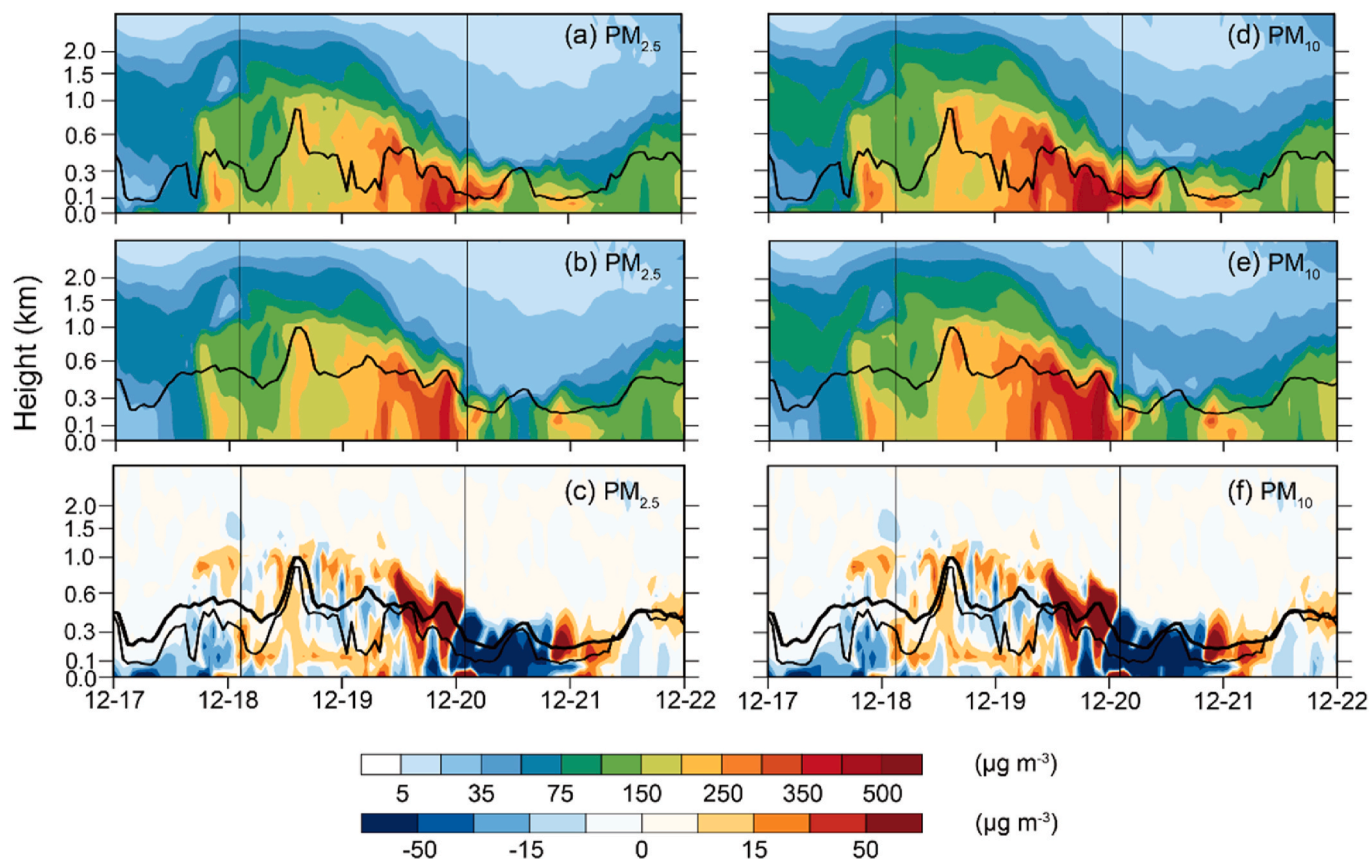

Fig. 11. Time series of the vertical profiles of simulated $PM_{2.5}$ concentration in urban areas of CLUA in (a) CTR case, (b) EXP case and (c) the difference of two cases, and of simulated PM_{10} concentration, in (d) CTR case, (e) EXP case and (f) the difference of two cases. The black solid lines in (a)–(b) and (d)–(e) show the simulated ABLH in each case. In (c) and (f), warm colors indicate higher PM concentration in EXP and cool colors indicate the opposite. The thinner and thicker black lines represent the ABLH in CTR case and EXP case, respectively.

4. Conclusion

In this study, the atmospheric chemical model WRF-Chem is applied to simulate the spatial and temporal distribution of atmospheric particulate matter and related meteorological variables during a heavy pollution process in CLUA, located in northeast China. A cluster of numerical sensitive experiments were also set up to analyze the effect of urbanized atmosphere-land surface process on the UHI effect and the spatial and temporal distribution of atmospheric particulate matter in and around the mega-city aggregation. The MSUCM was applied in the experiment (EXP) case to consider the inhomogeneous wind vertical profiles in the street canyon and its vertical diffusion mechanism of urban land surface process, while the SLUCM scheme in WRF was applied for control (CTR) case. By comparing both the EXP and CTR with the observed near-surface temperature, atmospheric boundary layer height and atmospheric particulate matter concentrations in the urban street, the main conclusions of the studies are as follows:

1. The temporal and spatial variations of urban heat island intensity (indicated by the difference in near-surface temperature between urban and suburban areas) and the decline rate of near-surface temperature during the nighttime in EXP case are more consistent with the observation than those in CTR. The NME of simulated TSK decreases from 1.20% in CTR case to 0.38% in EXP case during the nighttime. It indicated that the physical processing, especially the wind and diffusion mechanisms in and over the urban canopy, is key for a good-performant simulation of near-surface temperature in the case of air pollution in CLUA.

2. The urbanization results in more complex wind vertical profiles and land-surface energy budget and the vertical diffusion of near ground air pollutant. Then a higher near-surface temperature, stronger atmospheric turbulence, and an increase in the height of the atmospheric boundary layer over urban areas were simulated in the EXP simulation, especially during the nighttime, which is more coincident to the observation than those in CTR. The NME of the simulated ABLH and AEC decreases from 48.98% and 44.49% in CTR case to 24.95% and 24.21% in EXP case during the nighttime, respectively. Moreover, the higher AEC and the enhanced vertical mixing of the near-surface pollutants finally changed the near-ground concentrations during the air pollution events. The NME of the $PM_{2.5}$ and PM_{10} concentrations decreases from 43.22% and 23.71% in CTR to 32.82% and 18.57% in EXP case during the nighttime, with the value of r between $PM_{2.5}$ and PM_{10} concentrations by EXP and OBS increasing to 0.86 and 0.84, respectively.

3. Over the CLUA, the urban heat island effect is stronger in winter or during the nighttime. And it may affect the accumulation of local near-surface emissions in urban areas and regional transport from around regions of particulate pollution. In winter nights, the boundary layer height over the urban areas is higher than that over the suburbs. On the one hand, a higher mixing layer may be produced for the near-ground particulate pollution, thereby increasing the atmospheric environmental capacity. On the other hand, a more effective vertical transport may happen to the pollutants from the upside atmosphere to the urban near ground. Moreover, this urban heat island atmospheric circulation may be coupled with the other circulation, e.g., mountain-valley breeze caused by the surrounding topography, which results in a more complex lower atmospheric circulation as well as the spatial and temporal distribution of atmospheric pollutants in and surrounding the urban areas.

CRediT authorship contribution statement

Wenxi Zhang: Writing – original draft, Visualization, Validation, Software. **Zhenxin Liu:** Writing – review & editing, Software, Methodology, Funding acquisition, Conceptualization. **Xiaolan Li:** Resources, Methodology, Funding acquisition, Data curation. **Yuhao Mao:** Methodology, Data curation. **Yanjun Ma:** Validation, Project administration, Data curation. **Hong Liao:** Project administration, Funding acquisition.

Declaration of competing interest

The authors declare that they have no known competing financial interests or personal relationships that could have appeared to influence the work reported in this paper.

Appendix A. Supplementary data

Supplementary data to this article can be found online at https://doi.org/10.1016/j.atmosenv.2024.120866.

Data availability

The input data for simulation by WRF-Chem, as well as the observation and simulation of meteorological conditions and atmospheric pollutant concentrations for validation and analysis in this paper, are available at https://doi.org/10.5281/zenodo.10875363.

References

Banks, R.F., Tiana-Alsina, J., Baldasano, J.M., et al., 2016. Sensitivity of boundary-layer variables to PBL schemes in the WRF model based on surface meteorological observations, lidar, and radiosondes during the HygrA-CD campaign. Atmos. Res. 176–177, 185–201. https://doi.org/10.1016/j.atmosres.2016.02.024.

Cai, W.J., Li, K., Liao, H., et al., 2017. Weather conditions conducive to Beijing severe haze more frequent under climate change. Nat. Clim. Change 7 (4), 257–262. https://doi.org/10.1038/NCLIMATE3249.

Cheng, W.C., Porte-Agel, F., 2021. A simple mixing-length model for urban canopy flows. Boundary-Layer Meteorol. 181 (1), 1–9. https://doi.org/10.1007/s10546-021-00650-0.

Cheng, Y., Cao, X.B., Yu, Q.Q., et al., 2022. Synergy of multiple drivers leading to severe winter haze pollution in a megacity in Northeast China. Atmos. Res. 270, 106075. https://doi.org/10.1016/j.atmosres.2022.106075.

Chu, Y., Li, J., Li, C., et al., 2019. Seasonal and diurnal variability of planetary boundary layer height in Beijing: Intercomparison between MPL and WRF results. Atmos. Res. 227, 1–13. https://doi.org/10.1016/j.atmosres.2019.04.017.

Crutzen, P.J., 2004. New Directions: the growing urban heat and pollution "island" effect—impact on chemistry and climate. Atmos. Environ. 38 (21), 3539–3540. https://doi.org/10.1016/j.atmosenv.2004.03.032.

Daniel, M., Lemonsu, A., Déqué, M., et al., 2019. Benefits of explicit urban parameterization in regional climate modeling to study climate and city interactions. Clim. Dynam. 52 (5), 2745–2764. https://doi.org/10.1007/s00382-018-4289-x.

De Lange, A., Naidoo, M., Garland, R.M., et al., 2021. Sensitivity of meteorological variables on planetary boundary layer parameterization schemes in the WRF-ARW model. Atmos. Res. 247, 105214. https://doi.org/10.1016/j.atmosres.2020.105214.

Fan, H., Zhao, C.F., Yang, Y.K., 2020. A comprehensive analysis of the spatio-temporal variation of urban air pollution in China during 2014-2018. Atmos. Environ. 220, 117066. https://doi.org/10.1016/j.atmosenv.2019.117066.

Fang, C.L., Liu, H.M., Li, G.D., et al., 2015. Estimating the impact of urbanization on air quality in China using spatial regression models. Sustainability 7 (11), 15570–15592. https://doi.org/10.3390/su71115570.

Fu, H.B., Chen, J.M., 2017. Formation, features and controlling strategies of severe haze-fog pollution in China. Sci. Total Environ. 578, 121–138. https://doi.org/10.1016/j.scitotenv.2016.10.201.

Garuma, G.F., 2018. Review of urban surface parameterizations for numerical climate models. Urban Clim. 24, 830–851. https://doi.org/10.1016/j.uclim.2017.10.006.

Gu, Z.L., Zhang, Y.W., Cheng, Y., et al., 2011. Effect of uneven building layout on air flow and pollutant dispersion in non-uniform street canyons. Build. Environ. 46 (12), 2657–2665. https://doi.org/10.1016/j.buildenv.2011.06.028.

Guo, J., Miao, Y., Zhang, Y., et al., 2016. The climatology of planetary boundary layer height in China derived from radiosonde and reanalysis data. Atmos. Chem. Phys. 16 (20), 13309–13319. https://doi.org/10.5194/acp-16-13309-2016.

He, C., Zhou, L., Yao, Y., et al., 2020. Estimating spatial effects of anthropogenic heat emissions upon the urban thermal environment in an urban agglomeration area in East China. Sustain. Cities Soc. 57, 102046. https://doi.org/10.1016/j.scs.2020.102046.

He, Y.Y., Tablada, A., Wong, N.H., 2018. Effects of non-uniformand orthogonal breezeway networks on pedestrian ventilation in Singapore's high-density urban environments. Urban Clim. 24, 460–484. https://doi.org/10.1016/j.uclim.2017.03.005.

Huang, M., Gao, Z., Miao, S., et al., 2019. Sensitivity of urban boundary layer simulation to urban canopy models and PBL schemes in Beijing. Meteorol. Atmos. Phys. 131 (5), 1235–1248. https://doi.org/10.1007/s00703-018-0634-1.

Huo, Y., Wang, Y., Paasonen, P., et al., 2021. Trends of planetary boundary layer height over urban cities of China from 1980–2018. Front. Environ. Sci. 9, 744255. https://doi.org/10.3389/fenvs.2021.744255.

Kim, G., Lee, J.L., Lee, M.I., et al., 2021. Impacts of urbanization on atmospheric circulation and aerosol transport in a coastal environment simulated by the WRF-Chem coupled with urban canopy model. Atmos. Environ. 249, 118253. https://doi.org/10.1016/j.atmosenv.2021.118253.

Kusaka, H., Kondo, H., Kikegawa, Y., et al., 2001. A simple single-layer urban canopy model for atmospheric models: comparison with multi-layer and slab models. Boundary-Layer Meteorol. 101 (3), 329–358. https://doi.org/10.1023/A:1019207923078.

Lee, S.H., Park, S.U., 2008. A vegetated urban canopy model for meteorological and environmental modelling. Boundary-Layer Meteorol. 126 (1), 73–102. https://doi.org/10.1007/s10546-007-9221-6.

Li, B., Shi, X.F., Liu, Y.P., et al., 2020a. Long-term characteristics of criteria air pollutants in megacities of Harbin-Changchun megalopolis, Northeast China: spatiotemporal variations, source analysis, and meteorological effects. Environ. Pollut. 267, 115441. https://doi.org/10.1016/j.envpol.2020.115441.

Li, B., Zhou, S., Wang, T., et al., 2020b. Spatio-temporal distribution and influencing factors of atmospheric polycyclic aromatic hydrocarbons in the Yangtze River Delta. J. Clean. Prod. 267, 122049. https://doi.org/10.1016/j.jclepro.2020.122049.

Li, C.L., Liu, M., Hu, Y.M., et al., 2020c. Spatial distribution characteristics of gaseous pollutants and particulate matter inside a city in the heating season of Northeast China. Sustain. Cities Soc. 61, 102302. https://doi.org/10.1016/j.scs.2020.102302.

Li, G.D., Fang, C.L., Wang, S.J., et al., 2016. The effect of economic growth, urbanization, and industrialization on fine particulate matter ($PM_{2.5}$) concentrations in China. Environ. Sci. Technol. 50 (21), 11452–11459. https://doi.org/10.1021/acs.est.6b02562.

Li, X.L., Hu, X.M., Ma, Y.J., et al., 2019a. Impact of planetary boundary layer structure on the formation and evolution of air-pollution episodes in Shenyang, Northeast China. Atmos. Environ. 214, 116850. https://doi.org/10.1016/j.atmosenv.2019.116850.

Li, X.L., Ma, Y.J., Wei, W., et al., 2019b. Vertical distribution of particulate matter and its relationship with planetary boundary layer structure in Shenyang, northeast China. Aerosol Air Qual. Res. 19 (11), 2464–2476. https://doi.org/10.4209/aaqr.2019.06.0311.

Li, X.L., Wang, Y.F., Shen, L.D., et al., 2018. Characteristics of boundary layer structure during a persistent haze event in the central liaoning city cluster, northeast China. J. Meteorol. Res. 32 (2), 302–312. https://doi.org/10.1007/s13351-018-7053-6.

Li, Y., Zhao, X.G., Liao, Q., et al., 2020d. Specific differences and responses to reductions for premature mortality attributable to ambient $PM_{2.5}$ in China. Sci. Total Environ. 742, 140643. https://doi.org/10.1016/j.scitotenv.2020.140643.

Lin, Y.-L., Farley, R.D., Orville, H.D., 1983. Bulk parameterization of the snow field in a cloud model. J. Appl. Meteorol. Climatol. 22 (6), 1065–1092. https://doi.org/10.1175/1520-0450(1983)022<1065:BPOTSF>2.0.CO;2.

Liu, Y., Li, Q., Yang, L., et al., 2020. Urban heat island effects of various urban morphologies under regional climate conditions. Sci. Total Environ. 743, 140589. https://doi.org/10.1016/j.scitotenv.2020.140589.

Liu, Y.C., Zhao, H.J., Ma, Y.J., et al., 2021. Characteristics of particulate matter and meteorological conditions of a typical air-pollution episode in Shenyang, northeastern China, in winter 2017. Atmos. Pollut. Res. 12 (1), 316–327. https://doi.org/10.1016/j.apr.2020.09.007.

Liu, Z., 2013. Assessing the Urbanization Effects by Applying an Urban Canopy Model and Coupling it with Weather Research and Forecasting. Peking University, China, pp. 80–102. PHD thesis.

Liu, Z., Chen, Y., Wang, Y., et al., 2023. The development and validation of the inhomogeneous wind scheme for urban street (IWSUS-v1). Geosci. Model Dev. (GMD) 16 (15), 4385–4403. https://doi.org/10.5194/gmd-16-4385-2023.

Luan, T., Guo, X.L., Guo, L.J., et al., 2018. Quantifying the relationship between $PM_{2.5}$ concentration, visibility and planetary boundary layer height for long-lasting haze and fog-haze mixed events in Beijing. Atmos. Chem. Phys. 18 (1), 203–225. https://doi.org/10.5194/acp-18-203-2018.

Lv, Z., Wei, W., Cheng, S.Y., et al., 2020. Meteorological characteristics within boundary layer and its influence on $PM_{2.5}$ pollution in six cities of North China based on WRF-Chem. Atmos. Environ. 228, 117417. https://doi.org/10.1016/j.atmosenv.2020.117417.

Ma, Y., Liang, P., Grimmond, S., et al., 2022. Three-dimensional urban thermal effect across a large city cluster during an extreme heat wave: observational analysis. J. Meteorol. Res. 36 (3), 387–400. https://doi.org/10.1007/s13351-022-1171-x.

Ma, Y., Liu, Q., Bian, Y., et al., 2021a. Analysis of Transport Path and Source Distribution of Winter Air Pollution in Shenyang, vol. 13, pp. 1105–1117. https://doi.org/10.1515/geo-2020-0292, 1.

Ma, Y.F., Wang, M.B., Wang, S., et al., 2021b. Air pollutant emission characteristics and HYSPLIT model analysis during heating period in Shenyang, China. Environ. Monit. Assess. 193 (1), 9. https://doi.org/10.1007/s10661-020-08767-4.

Masson, V., 2000. A physically-based scheme for the urban energy budget in atmospheric models. Boundary-Layer Meteorol. 94 (3), 357–397. https://doi.org/10.1023/A:1002463829265.

Meng, C., Huang, C., Dou, J., et al., 2021a. Key parameters in urban surface radiation budget and energy balance modeling. Urban Clim. 39, 100940. https://doi.org/10.1016/j.uclim.2021.100940.

Meng, C.S., Tang, Q., Yang, Z.H., et al., 2021b. Collaborative control of air pollution in the Beijing-Tianjin-Hebei region. Environ. Technol. Innovat. 23, 101557. https://doi.org/10.1016/j.eti.2021.101557.

Myrup, L.O., 1969. A numerical model of the urban heat island. J. Appl. Meteorol. Climatol. 8 (6), 908–918. https://doi.org/10.1175/1520-0450(1969)008<0908:ANMOTU>2.0.CO;2.

Nakanishi, M., Niino, H., 2009. Development of an improved turbulence closure model for the atmospheric boundary layer. J. Meteorol. Soc. Japan. Ser. II 87 (5), 895–912. https://doi.org/10.2151/jmsj.87.895.

Offerle, B., Eliasson, I., Grimmond, C.S.B., et al., 2007. Surface heating in relation to air temperature, wind and turbulence in an urban street canyon. Boundary-Layer Meteorol. 122 (2), 273–292. https://doi.org/10.1007/s10546-006-9099-8.

Rafael, S., Martins, H., Marta-Almeida, M., et al., 2017. Quantification and mapping of urban fluxes under climate change: application of WRF-SUEWS model to Greater Porto area (Portugal). Environ. Res. 155, 321–334. https://doi.org/10.1016/j.envres.2017.02.033.

Rutledge, S.A., Hobbs, P.V., 1984. The mesoscale and microscale structure and organization of clouds and precipitation in midlatitude cyclones. XII: A diagnostic modeling study of precipitation development in narrow cold-frontal rainbands. J. Atmos. Sci. 41 (20), 2949–2972. https://doi.org/10.1175/1520-0469(1984)041<2949:TMAMSA>2.0.CO;2.

Ryu, Y.H., Baik, J.J., Lee, S.H., 2011. A new single-layer urban canopy model for use in mesoscale atmospheric models. J. Appl. Meteorol. Climatol. 50 (9), 1773–1794. https://doi.org/10.1175/2011JAMC2665.1.

Schell, B., Ackermann, I.J., Hass, H., et al., 2001. Modeling the formation of secondary organic aerosol within a comprehensive air quality model system. J. Geophys. Res. Atmos. 106 (D22), 28275–28293. https://doi.org/10.1029/2001JD000384.

Shi, T., Liu, M., Hu, Y.M., et al., 2019. Spatiotemporal pattern of fine particulate matter and impact of urban socioeconomic factors in China. Int. J. Environ. Res. Publ. Health 16 (7), 1099. https://doi.org/10.3390/ijerph16071099.

Stockwell, W.R., Middleton, P., Chang, J.S., et al., 1990. The second generation regional acid deposition model chemical mechanism for regional air quality modeling. J. Geophys. Res. Atmos. 95 (D10), 16343–16367. https://doi.org/10.1029/JD095iD10p16343.

Su, T.N., Li, Z.Q., Kahn, R., 2018. Relationships between the planetary boundary layer height and surface pollutants derived from lidar observations over China: regional pattern and influencing factors. Atmos. Chem. Phys. 18 (21), 15921–15935. https://doi.org/10.5194/acp-18-15921-2018.

Sun, Y., Zhang, N., Miao, S.G., et al., 2021. Urban morphological parameters of the main cities in China and their application in the WRF model. J. Adv. Model. Earth Syst. 13 (8), e2020MS002382. https://doi.org/10.1029/2020MS002382.

Tam, B.Y., Gough, W.A., Mohsin, T., 2015. The impact of urbanization and the urban heat island effect on day to day temperature variation. Urban Clim. 12, 1–10. https://doi.org/10.1016/j.uclim.2014.12.004.

Vogelezang, D.H.P., Holtslag, A.a.M., 1996. Evaluation and model impacts of alternative boundary-layer height formulations. Boundary-Layer Meteorol. 81 (3), 245–269. https://doi.org/10.1007/BF02430331.

Wang, C.H., Wang, Z.H., Ryu, Y.H., 2021a. A single-layer urban canopy model with transmissive radiation exchange between trees and street canyons. Build. Environ. 191, 107593. https://doi.org/10.1016/j.buildenv.2021.107593.

Wang, H., Liu, Z., Zhang, Y., et al., 2021b. Impact of different urban canopy models on air quality simulation in Chengdu, southwestern China. Atmos. Environ. 267, 118775. https://doi.org/10.1016/j.atmosenv.2021.118775.

Wang, Z.B., Fang, C.L., 2016. Spatial-temporal characteristics and determinants of $PM_{2.5}$ in the Bohai rim urban agglomeration. Chemosphere 148, 148–162. https://doi.org/10.1016/j.chemosphere.2015.12.118.

Yang, D.Y., Chen, Y.L., Miao, C.H., et al., 2020a. Spatiotemporal variation of $PM_{2.5}$ concentrations and its relationship to urbanization in the Yangtze river delta region, China. Atmos. Pollut. Res. 11 (3), 491–498. https://doi.org/10.1016/j.apr.2019.11.021.

Yang, H.M., Peng, Q., Zhou, J., et al., 2020b. The unidirectional causality influence of factors on $PM_{2.5}$ in Shenyang city of China. Sci. Rep. 10 (1), 8403. https://doi.org/10.1038/s41598-020-65391-5.

Yang, J., Wang, z.-H., Chen, F., et al., 2015. Enhancing hydrologic modelling in the coupled weather research and forecasting–urban modelling system. Boundary-Layer Meteorol. 155 (1), 87–109. https://doi.org/10.1007/s10546-014-9991-6.

Yang, Q., Huang, X., Tang, Q., 2019. The footprint of urban heat island effect in 302 Chinese cities: temporal trends and associated factors. Sci. Total Environ. 655, 652–662. https://doi.org/10.1016/j.scitotenv.2018.11.171.

Yin, J., Gao, C.Y., Hong, J., et al., 2019. Surface meteorological conditions and boundary layer height variations during an air pollution episode in nanjing, China. J. Geophys. Res. Atmos. 124 (6), 3350–3364. https://doi.org/10.1029/2018JD029848.

Zhang, J., Liu, L., Wang, Y.Y., et al., 2017. Chemical composition, source, and process of urban aerosols during winter haze formation in Northeast China. Environ. Pollut. 231, 357–366. https://doi.org/10.1016/j.envpol.2017.07.102.

Zhang, J., Liu, L., Xu, L., et al., 2020. Exploring wintertime regional haze in northeast China: role of coal and biomass burning. Atmos. Chem. Phys. 20 (9), 5355–5372. https://doi.org/10.5194/acp-20-5355-2020.

Zhang, L.L., Zhao, N., Zhang, W.H., et al., 2022. Changes in long-term $PM_{2.5}$ pollution in the urban and suburban areas of China's three largest urban agglomerations from 2000 to 2020. Rem. Sens. 14 (7), 1716. https://doi.org/10.3390/rs14071716.

Zhang, X.Y., Wang, L., Wang, W.H., et al., 2015. Long-term trend and spatiotemporal variations of haze over China by satellite observations from 1979 to 2013. Atmos. Environ. 119, 362–373. https://doi.org/10.1016/j.atmosenv.2015.08.053.

Zhao, H.J., Che, H.Z., Zhang, L., et al., 2020. How aerosol transport from the North China plain contributes to air quality in northeast China. Sci. Total Environ. 738, 139555. https://doi.org/10.1016/j.scitotenv.2020.139555.

Zhao, H.J., Che, H.Z., Zhang, X.Y., et al., 2013. Characteristics of visibility and particulate matter (PM) in an urban area of Northeast China. Atmos. Pollut. Res. 4 (4), 427–434. https://doi.org/10.5094/APR.2013.049.

Zhou, D.C., Sun, S.L., Li, Y., et al., 2023. A multi-perspective study of atmospheric urban heat island effect in China based on national meteorological observations: facts and uncertainties. Sci. Total Environ. 854, 158638. https://doi.org/10.1016/j.scitotenv.2022.158638.

Zhu, L., Huang, Q.X., Ren, Q., et al., 2020. Identifying urban haze islands and extracting their spatial features. Ecol. Indicat. 115, 106385. https://doi.org/10.1016/j.ecolind.2020.106385.